Building and Environment 135 (2018) 124–141

Contents lists available at ScienceDirect

Building and Environment

journal homepage: www.elsevier.com/locate/buildenv

Numerical investigation of a swirl diffuser with a novel design using large eddy simulations

Zhenqing Liu[a,*], Qiuming Li[a], Takeshi Ishihara[b]

[a] School of Civil Engineering and Mechanics, Huazhong University of Science & Technology, Wuhan, Hubei, China
[b] Department of Civil Engineering, School of Engineering, The University of Tokyo, Tokyo, Japan

ARTICLE INFO

Keywords:
Swirl diffuser
Numerical simulation
Aging
Large eddy simulation
Axial velocity

ABSTRACT

In the present study, a swirl diffuser with a novel design is proposed, in which three geometrical parameters, the angle of the guide vanes φ, the height of the convergent chamber h, and the radius of the diffuser outlet r, can be varied independently. Large eddy simulations were conducted to examine the airflow characteristics downstream of the swirl diffuser. Grid independence was obtained for the grid number 4000,000, and this result was validated by comparison with an experiment. The vorticities, the instantaneous and averaged velocities, and the evolution of the age of air were investigated. The turbulent kinetic energy budget and the momentum balance in the time-averaged Navier–Stokes equations were then studied in an attempt to clarify the mechanism of the swirl diffuser's high diffusing performance. With the increasing swirling strength, the pressure gradient force could not balance the centrifugal force in the radial direction. As a result, the vortex core expanded, generating turbulence. A non-dimensional swirl number parameter was suggested which can be used for determining the structure of the swirl diffuser airflow. To validate this non-dimensional parameter, different combinations of φ, h, and r were examined. It was found that only if the swirl number is the same, will the airflow structure be similar. The results of our study are likely to be useful for obtaining deeper insights about the swirl diffuser airflow, and for better understanding of the effect of the controlling parameter on the swirl diffuser's performance.

1. Introduction

In the microelectronics industry, medical device industry, and biotechnology industry, the indoor air quality (IAQ) is required to be high.

To improve the IAQ, researchers have developed several kinds of diffusers, such as square diffusers [1–4], round diffusers [5,6], and swirl diffusers [7–13]. Among these, swirl diffusers have been receiving increasing attention of researchers, not only owing to their diffusion efficiency but also owing to their low energy consumption. During the last decade, several experimental and numerical examinations of the performance of swirl diffusers have been conducted, in which the flow structures, the diffusion efficiency, and the optimization of their geometrical parameters have been studied; these studied have yielded some valuable insights. In what follows, we briefly review these previous research accomplishments.

Experimentation is the most direct way to study the airflows generated by swirl diffusers. However, owing to the difficulties associated with the measurement of flow fields, experimental studies of swirl diffusers are scarce [7–9]. Most of the relevant experimental studies of swirl diffusers used spatially localized measurements to analyze the airflow patterns of swirl diffusers [7,8]. However, without the global-scale information about the analyzed flow field, the flow structure cannot be revealed. Therefore, Li et al. [10] applied a two-dimensional particle image velocimetry (2D-PIV) technique to study the air distribution performance of a swirl diffuser in a full-scale room under isothermal conditions. Using flow visualization and PIV technology, the macro- and micro-level structures of the air flow above the swirl diffuser were determined. A strong rotation in a central area near the swirl diffuser's outlet was obvious. In addition, a contraction was observed at the horizontal section. By examining the jet centerline velocity decay coefficient and entrainment ratio, it was concluded that the swirl diffuser exhibited significant diffusion effects compared with ceiling diffusers. However, the 2D-PIV technique did not provide a full picture of the three-dimensional (3D) flow fields downstream of the swirl diffuser. The statistical information about the flow fields obtained using the 2D-PIV technique was limited to a two-dimensional (2D) plane, which is not sufficient to study the momentum balance of the Navier–Stokes equations and the turbulent kinetic energy (TKE) budget, in which the spatial gradients of velocities and turbulent stresses normal to the plane are also involved. Momentum balance and TKE budget are important

* Corresponding author.
E-mail address: liuzhenqing@hust.edu.cn (Z. Liu).

https://doi.org/10.1016/j.buildenv.2018.02.045
Received 27 November 2017; Received in revised form 6 February 2018; Accepted 26 February 2018
Available online 08 March 2018
0360-1323/

Nomenclature

C	CFL number
C_s	Smagorinsky constant
C_z	entrainment ratio
E	kinetic energy [m^2s^{-2}]
h	height of chamber [m]
k	turbulence kinetic energy [m^2s^{-2}]
K	jet centerline velocity decay coefficient
n	normal direction
N	node number
p	pressure [Nm^{-2}]
Q	flow rate [m^3s^{-1}]
r	radius of swirl diffuser outlet [m]
r'	radius of chamber [m]
R, Θ, Z	coordinate components in cylindrical coordinate system [ms^{-1}]
Re	Reynolds number
s	user defined scalar
S_n	swirl number
S_o	density of the age of air at room outlet [m^{-2}]
S_t	density of the age of air in the room [m^{-3}]
u,v,w	velocity components in Cartesian coordinate system [ms^{-1}]
U,V,W	velocity components in cylindrical coordinate system [ms^{-1}]
V_{in}	velocity at inlet [ms^{-1}]
x,y,z	coordinate components in Cartesian coordinate system [m]

Greek symbols

α	maximal grid increasing ratio
ε	computational error
λ_2	second eigenvalue of M
φ	angle of guide vanes [°]

Abbreviations

AMG	Algebraic Multi-Grid
CFD	computational fluids dynamics
CFL	Courant Friedrichs Lewy
DNS	direct numerical simulation
FVM	finite volume method
IAQ	indoor air quality
LES	large eddy simulations
N-S	Navier–Stokes
PIV	particle image velocimetry
RANS	Reynolds Averaged Navier–Stokes
rms	root mean square
SGS	subgrid-scale
TKE	turbulent kinetic energy
UFAD	underfloor air distribution
UDS	user defined scalar
UDF	user defined functions

Subscripts

-	mean values
’	rms
~	filtered values

for understanding the mechanism underlying the good performance of swirl diffusers.

Computational fluids dynamics (CFD) is a numerical approach that allows to obtain complete information of the flow fields. Nielsen [14,15] was one of the pioneers in using CFD methods to predict air movement and heat transfer in buildings. Without any doubt, predicting for indoor HVAC (Heating, Ventilation and Air Conditioning) by means of CFD has contributed to advances in HVAC system design [16–22]. The existing computational approaches to study swirl diffusers can be roughly categorized into two groups, based on their turbulence models: 1) Reynolds averaged Navier–Stokes (RANS) models [7,9,11–13,23], and 2) large eddy simulation (LES) models [24].

In RANS models, additional governing equations are needed to close the Reynolds averaged equations where additional unknown variables of the Reynolds stresses emerge. To study the airflow of swirl diffusers, the k-ε turbulence model, in which the k and ε equations are used to obtain the closure, has been widely used. Hu [9] studied the airflow characteristics in the outlet region of a swirl diffuser numerically, using the standard k-ε turbulence model. To capture the complex geometry of the swirl diffuser, a zonal hybrid mesh system was adopted around the diffuser. Numerical results were validated by comparison to experimental results, and the two were in a good agreement. It was also found that the swirl diffuser exhibits a larger entrainment ratio than a multi-cone circular ceiling diffuser. Sajadi et al. [12] also adopted the standard k-ε turbulence model to investigate a swirl diffuser and optimize its geometrical parameters. They found that the optimized angle of the blade is almost independent of the airflow rate. Most recently, Yau et al. [13] numerically studied the airflow pattern of a floor swirl diffuser for an underfloor air distribution (UFAD) system, using the standard k-ε turbulence model. In that study, the effects from the airflow rate, the number of the diffuser blades, the angle of the attack of the diffuser blades, and the grille thickness were examined. The results showed that the most important parameter determining the flow structure is the diffuser blade angle. However, in those studies, only the mean flow fields k and ε were calculated, while instantaneous flow fields and high-order Reynolds stresses, such as $\overline{u_i'u_j'u_k'}$, could not be determined.

Table 1
Previous numerical studies about swirling diffuser.

Authors	Time	Turbulence model	Steady or Unsteady	Age of air	Thermal performance	Axial velocity	TKE budget	Momentum balance
Aziz et al. [7]	2012	k-ε	Steady	○	○	○	×	×
Hu [9]	2003	k-ε	Steady	○	×	○	×	×
Wang and Pepper [11]	2007	k-ε	Steady	×	○	○	×	×
Sajadi et al. [12]	2011	k-ε	Steady	○	×	○	×	×
Yau et al. [13]	2017	k-ε	Steady	×	○	○	×	×
Tavakoli and Hosseini [24]	2013	LES	Unsteady	○	×	○	×	×
Present	2017	LES	Unsteady	○	×	○	○	○

○ means yes, × means no.

Nevertheless, high-order Reynolds stresses are necessary for calculating the TKE budget.

In LES models, a subgrid scale (SGS) model is needed to close the cell space averaged Navier–Stokes equations. With the increasing computational power and ability to obtain transient flow features and to provide more accurate results, large eddy simulations have been widely used in industrial applications, even though LES models are more expensive than RANS models. To the best of our knowledge, only one study used LES to model the indoor swirl diffuser airflow, namely the study by Tavakoli and Hosseini [24]. In that study, transient flow structures, mass transfer and ventilation characteristics in the far-field of swirl diffusers were studied, and three types of secondary flow structures were observed. The total aging was found to be the minimal when the swirl angle was ~55°. However, the ability to examine the dimensionless parameters that determine the flow patterns is limited, which is important for design and control of swirl diffusers. The numerical studies are summarized in Table 1.

In the present study, a swirl diffuser with a novel design is proposed, in which three parameters, the angle of the guide vanes φ, the height of the convergent chamber h, and the radius of the diffuser outlet r, can be controlled independently. Large eddy simulations are performed to yield deeper insights about the flow structure and the mechanism of the effective diffusion properties of the proposed swirl diffuser. Section 2 presents the numerical model, including the governing equations, geometry, mesh, boundary conditions, and the solution schemes. The numerical results are presented in Section 3, including the vortical structures of the flow, the axial velocity and the age of air, the TKE budget, and the momentum balance. Finally, the dimensionless parameter, the swirl number, is discussed in Section 4.

2. Numerical model

The governing equations and configurations for the numerical model of the swirl diffuser are introduced in Section 2.1 and Section 2.2, followed by the presentation of the system's boundary conditions and case parameters used in this study. The numerical solution scheme is described as well.

2.1. Governing equations

Momentum and mass are primarily transported by large eddies; therefore, a LES approach is usually adopted to simulate the airflow around swirl diffusers. In such simulations, large eddies are directly computed, while the influence of eddies smaller than the grid spacing is parameterized. From the computational efficiency viewpoint, the LES approach is between the RANS approach that has been used in many swirl diffuser studies [7,9,11–13,23] and the direct numerical simulation (DNS) approach, and its use is motivated by the limitations of each of the latter two approaches. Because large-scale unsteady motion is represented explicitly, the LES approach can be expected to be more accurate and reliable than the RANS method for flows in which large-scale unsteadiness is significant — such as the flows associated with swirl diffusers that involve unsteady vortex evolution. The Boussinesq hypothesis is employed. In the studies [25,26] the standard Smagorinsky–Lilly model [27,28] has been proved to be a satisfactory SGS model and is applied also in the present study.

The governing equations are obtained by filtering the time-dependent Navier–Stokes equations in Cartesian coordinates (x, y, z), which can be expressed as follows:

$$\frac{\rho\partial\tilde{u}_i}{\partial x_i} = 0 \tag{1}$$

$$\frac{\rho\partial\tilde{u}_i}{\partial t} + \frac{\rho\partial\tilde{u}_i\tilde{u}_j}{\partial x_j} = \frac{\partial}{\partial x_j}\left(\mu\frac{\partial\tilde{u}_i}{\partial x_j}\right) - \frac{\partial\tilde{p}}{\partial x_i} - \frac{\partial\tau_{ij}}{\partial x_j} \tag{2}$$

where $\tilde{u}_i$ and $\tilde{p}$ are the filtered velocities (u, v, w) and pressure, respectively, μ is the viscosity, ρ is the density, and τ_{ij} is the SGS stress. To close the equation for the filtered velocity, a model for the anisotropic residual stress tensor τ_{ij} is needed, which is modeled as follows [29]:

$$\tau_{ij} = -2\mu_t\tilde{S}_{ij} + \frac{1}{3}\tau_{kk}\delta_{ij} \tag{3}$$

$$\tilde{S}_{ij} = \frac{1}{2}\left(\frac{\partial\tilde{u}_i}{\partial x_j} + \frac{\partial\tilde{u}_j}{\partial x_i}\right) \tag{4}$$

where μ_t denotes the SGS turbulent viscosity, $\tilde{S}_{ij}$ is the rate-of-strain tensor for the resolved scale, and δ_{ij} is the Kronecker delta. The Smagorinsky–Lilly model is used for the SGS turbulent viscosity:

$$\mu_t = \rho L_s^2|\tilde{S}| = \rho L_s^2\sqrt{2\tilde{S}_{ij}\tilde{S}_{ij}} \tag{5}$$

$$L_s = min(\kappa d,\ C_s V^{1/3}) \tag{6}$$

in which L_s denotes the SGS mixing length, κ is the von Kármán constant, i.e., 0.42, d is the distance to the closest wall, and V is the volume of a computational cell. In this study, C_s is the Smagorinsky constant. As has been suggested by Karniadakis and Sherwin [30] and applied in LES studies [31,32] about diffusers as well as the studies about the fully developed turbulent flows by Liu et al. [25,26], C_s is determined to be

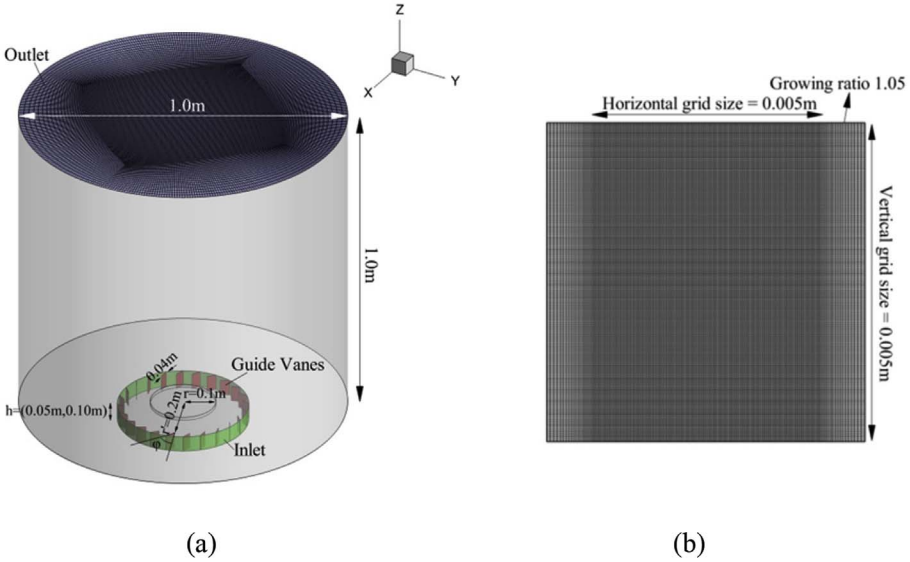

Fig. 1. Configurations of the computational domain (a) and mesh on the vertical slice (b). The blue area with transparent effect is the outlet of the room, the red area guide vanes and green area inlet. Horizontal mesh distribution in the room is illustrated at the outlet of room which is not changed along the whole room domain. (For interpretation of the references to color in this figure legend, the reader is referred to the Web version of this article.)

0.1.

2.2. Computational domain and mesh

The computational domain used in this study is shown schematically in Fig. 1. Different from the swirl diffusers examined in previous studies [7–13,23,24], in the present study the swirl diffuser consisted of a chamber (with radius (r') = 0.2 m, radius of outlet (r) = 0.1 m, height (h) = 0.05 m and 0.10 m), and guide vanes (with height (h) equaling to that of the chamber). The angle of the guide vanes (φ) could be adjusted to change the swirling strength of the flow; as a result, different types of flow structures could be produced. In the presently designed swirl diffuser, the height of the chamber, the chamber outlet radius, and the angle of the guide vanes could be controlled independently, expanding the applicability scope. For example, in some situations the chamber outlet radius, the angle of the guide vanes, and the flow rate cannot be easily changed, but to provide a different airflow speed at a certain location, the height of the chamber can be adjusted. This occurs because changing the height of the chamber changes the swirling strength; this will be further clarified in the following discussion on the dimensionless parameter, the swirl number (S_n). A room with a radius = 1.0 m and height = 1.0 m was chosen for those studies. The geometrical parameters are listed in Table 2. The Cartesian coordinates system (x, y, z) is defined by the axis as in Fig. 2(a). This system of coordinates was used for solving the governing equations, where the origin ($x = 0, y = 0, z = 0$) was at the center of the chamber outlet. The corresponding instantaneous velocities were u, v, and w, respectively. (Quantities with top bars, such as $\overline{u}$, $\overline{v}$, $\overline{w}$, refer to the average values, while quantities with primes, such as u', v', w', denote the root mean square (rms) values.) The cylindrical coordinates system (R, Θ, Z), where R is in the radial direction, Θ is in the azimuthal direction, and Z is in the vertical direction, will be used for the following momentum balance analysis (Fig. 2(b)), where the origin ($R = 0, \Theta = 0, Z = 0$) is also at the center of the chamber outlet. The corresponding instantaneous axial, radial, and tangential velocities are U, V, and W. (Quantities with top bars, such as $\overline{U}$, $\overline{V}$, $\overline{W}$, refer to the average values, while quantities with primes, such as U', V', W', denote the rms values.)

Owing to the simple design of the present swirl diffuser, using a block-structured mesh system becomes possible. A hexahedron grid was adopted for the entire computational domain, including the region near the guide vanes. The central part of the computational mesh was made up entirely of 3D hexahedron elements following the work by Aziz [7], Sajadi [12], From Ref. [33], Valera [34], Bounous [35]. A standard O-H grid on the circumferential faces (Fig. 1(a) and (b)) was applied. Cubic meshes with edges equaling 5 mm were used for the central section, whose width was 0.7 m. Close to the cylindrical walls of the room, the size of the horizontal mesh was increased to 10 mm at the growth ratio $\alpha = 1.05$, as shown in Fig. 1(b), to avoid a sudden change in the grid size. These grid size parameters were taken from mesh independence studies, as listed in Table 3, where N was the number of nodes and N was systematically decreased in steps of 2. A detailed description of grid independence and validation will be given in Section3.1. Grid independence was attained when the number of grid points was $\sim 4.0 \times 10^6$. Gambit is adopted to generate the mesh.

2.3. Boundary conditions

The green surface in Fig. 1(a) indicates the inlet of the domain where the velocity inlet boundary condition was applied. In the present study the velocity normal to the inlet, V_{in}, was set to 0.5 ms^{-1} when h = 0.05 m, and to 0.25 ms^{-1} when h = 0.10 m, respectively, so as to yield the same flow rate Q = 0.031 m^3s^{-1} and mean axial velocity at the swirl diffuser's outlet W_0 = 1.0 ms^{-1}. The normal gradient of pressure at the inlet was zero ($\partial p/\partial n = 0$). The guide vanes, the top and the bottom of the chamber, as well as the side walls of the room were set as wall boundary conditions where the velocities and the normal gradient of pressure were zero ($u_i = 0, \partial p/\partial n = 0$). At the outlet, same as in the study of Hu [9], the pressure outlet boundary condition was used, which means that the gradients of velocities and pressure were zero ($\partial u_i/\partial n = 0, \partial p/\partial n = 0$). Note that at the walls of the computational domain, y^+ values did not meet the common requirement, $y^+ < 1.0$, for large eddy simulations. However, the walls of the computational domain were not the regions of concern and the separations or the reattachments of the flow were not the goals of this study either. There likely were some effects associated with the turbulence generation from the walls in the chamber, but these effects were limited. Based on the following validation case (straight-line jet flow case, Case0) it was found that the neglect of y^+ at the walls was acceptable and the modeled mean axial flow as well as the turbulence intensities were almost the same as in the experiments. The boundary conditions are summarized in Table 4.

2.4. Case settings

Twelve cases, including four verification cases, were numerically simulated, as listed in Table 5. Considering the fact that there are many experimental and numerical studies of straight-line jet flows, Case0 with zero guide vane angles was used for validating the numerical settings and for grid independence examinations. In Cases 1–4 the height of the chamber was the same but the guide vane angle ranged from 3° to 73°. The swirl number, $S_n = tan\varphi/(2h/r)$, whose definition will be discussed in Section 4, ranged from 0.05 to 3.00. Cases 1′–4′ corresponded to Cases 1–4, with different chamber heights and guide vane angles. However, the swirl number was the same as for the corresponding cases, for the sake of checking if the swirl number was the non-dimensional parameter determining the swirl diffuser airflow structure.

2.5. Solution scheme and solution procedure

The finite volume method (FVM) was used in the simulations in which the variables were distributed in a non-staggered, cell-centered mesh system. The second-order central difference scheme was used for the convective and viscous terms, and the second-order implicit scheme was employed for the unsteady term:

$$\left(\frac{d\phi}{dt}\right)_n = \frac{3\phi^n - 4\phi^{n-1} + \phi^{n-2}}{2\Delta t_n}, \quad \Delta t_n = t - t_{n-1} = t_{n-1} - t_{n-2} \tag{7}$$

where the indices "n" and "n-1" denote the new and old time instances, respectively. The size of the time step Δt was 0.0001 s, and in convective time units it was $\Delta t^* = \Delta t W_0/r = 0.001$. The solution method consisted of linearizing the non-linear equations and implementing a matrix solution. The predicted conjugate gradient (PCG) method was applied to solve the linearized equations along with the algebraic multigrid (AMG) approach. The Courant–Friedrichs–Lewy [36] (CFL) number was based on the time step size (Δt), velocity (u_i), and grid size (Δx_i), and was expressed as $C = \Delta t \Sigma u_i/\Delta x_i$. Here, the CFL number was limited to not exceed 2, $C_{max} = 2$, in the entire computational domain. Reynolds number of the fluid is defined as $Re = W_0 r/\upsilon$ and equal to 1×10^5. The semi-implicit pressure linked equations (SIMPLE) algorithm was used to solve the discretized equations, which was

Table 2
Geometrical Parameters of the computational domain.

Radius of chamber (r') (m)	Outlet radius of chamber (r) (m)	Radius of room (l) (m)	Height of room (H) (m)
0.2	0.1	0.5	1.0

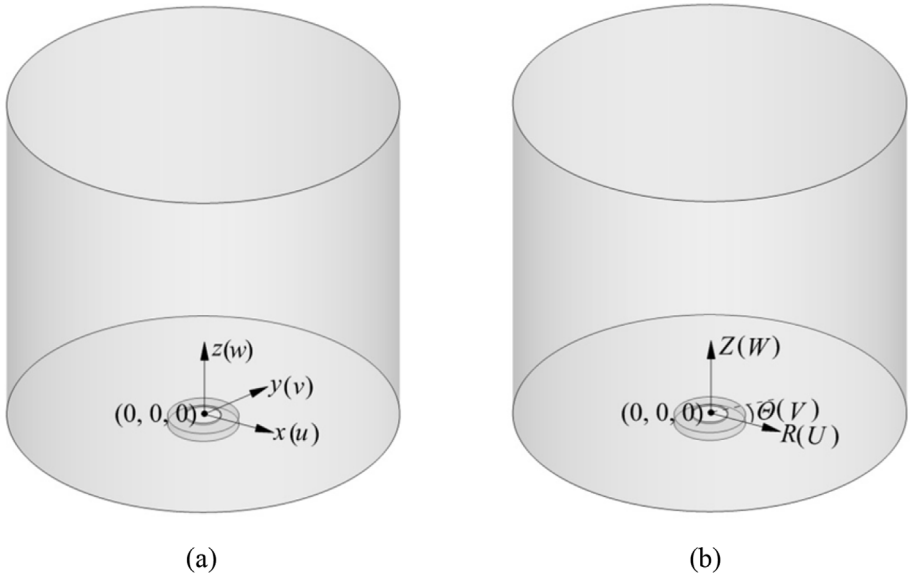

Fig. 2. Coordinate systems applied in the present study. (a) Cartesian coordinate system and (b) cylindrical coordinate system. The solid points indicate the origin of the coordinate systems.

introduced by Ferziger and Peric [29]. Relaxation factors were employed to promote the stability of the process. These relaxation factors were 0.3 and 0.7 for pressure and momentum, respectively. Commercial software Ansys Fluent 14.5 [37] was used for the calculations.

The initial transient effects were found to disappear after 5 s. Therefore, time sampling started at 10 s and then the flow fields were averaged temporally from 10 s to 30 s. A stationary condition for time sampling was determined by evaluating relative errors in the axial velocity at the point ($x = 0$, $y = 0$, $z = 0.5$ m) $V_{0.5}$, which was under 1% when the data from 10 s to 30 s were used. The time sampling error was calculated by determining the difference between the time-averaged result of $V_{0.5}$ from 10 s to 10 s + $T/2$, and from 10 s + $T/2$ to 10 s + T, where T was the time used for time sampling. The simulations for different cases were performed on different personal computers (PCs) (Intel Core i9-7980XE, 18 cores, 64 G memory). Thirty seconds of simulation time took from 245 h to 467 h of real time, as listed in Table 5. For larger swirl numbers, more computational recourses were needed, implying that the simulated flow's spatial and temporal gradients became steeper. Numerical schemes are summarized in Table 6.

3. Numerical results

In this section, the grid independence and validation of the numerical results are firstly presented. Then, the flow fields for Cases 1–4 are examined to clarify the effects from the swirling of the flow. The vortex structures are shown to provide the general characteristics of the instantaneous flow fields qualitatively. Then, the instantaneous vertical velocities, w, and the averaged (over time and Θ) ones, $\overline{w}$, are analyzed. Besides, the jet centerline velocity decay coefficient (K) and air entrainment ratio (C_z) are discussed to provide detailed quantitative information about the flow fields and the performance of the proposed swirl diffuser, followed by the introduction of the age of air, including the total aging in the room and that at the outlet of the room. Finally, the kinetic energy budget as well as the momentum balance of the Reynolds averaged Navier–Stokes equation in the cylindrical coordinates system (R, Θ, Z) are examined trying to clarify the mechanism underlying the high performance of the swirl diffuser.

Table 4
Settings for the boundary conditions.

Locations	Boundary type	Expression
Outlet of the room	Pressure outlet	$\partial u_i/\partial n = 0$, $\partial p/\partial n = 0$
Surrounding walls of the room	Non-slip wall	$\partial p/\partial n = 0$, $u_i = 0$
Inlet of the chamber	Velocity inlet	$V_{in} = 0.5\text{ms}^{-1}$, $\partial p/\partial n = 0$
Guide vanes	Non-slip wall	$\partial p/\partial n = 0$, $u_i = 0$
Surrounding walls of the chamber	Non-slip wall	$\partial p/\partial n = 0$, $u_i = 0$

3.1. Grid independence and validations

Overall, four increasingly refined grids, from Case 0–1 to Case 0–4, whose grid parameters are listed in Table 3, were constructed to conduct grid convergence tests and to determine mesh independence. In the present mesh independence studies, the grid number varied twofold, from the coarsest mesh to the finest mesh. Except the grid density, other settings, such as the solution scheme, boundary conditions, and initial values, were all the same. The mean vertical velocity and the rms of the vertical velocity along the central line (in the Cartesian coordinates system $x = 0$, $y = 0$; in the cylindrical coordinates system $r = 0$) from $z = 0$ to $z = 10r$ were compared for different mesh densities (Fig. 3). Superimposed in Fig. 3(a) and (b) are the experimental data from the study of Burattini et al. [38], fitted using the spline curves

Table 3
Grid parameters of the numerical model.

Grid type	Verification case	Minimum grid size (m)	Maximum grid size (m)	Grid Number N	Maximum Grid increasing ratio α
Cubit in the room and Hexahedron grid in the chamber	Case0-1	10.0 mm	20 mm	$\approx 5.0 \times 10^5$	1.05
	Case0-2	7.9 mm	15.8 mm	$\approx 1.0 \times 10^6$	1.05
	Case0-3	6.3 mm	12.6 mm	$\approx 2.0 \times 10^6$	1.05
	Case0-4	5.0 mm	10 mm	$\approx 4.0 \times 10^6$	1.05

Table 5
Case settings and computational resources.

Case name	Flow rate	Mean axial velocity at chamber outlet	Height of chamber	Reynolds number	Swirl number	Angle of inflow	Grid number	Computational time	CPU	Memory
	Q (m^3s^{-1})	W_0 (ms^{-1})	h (m)	$Re = W_0 r/\upsilon$	$S_n = \frac{tan\varphi}{2h/r}$	φ (°)	N	(Hours)		
Case0-1	0.031 $m^3 s^{-1}$	1 m s^{-1}	0.10	1×10^5	0.0	0°	0.5×10^6	20	Intel core	64G
Case0-2	0.031m^3s^{-1}	1 ms^{-1}	0.10	1×10^5	0.0	0°	1×10^6	42	i9-7980XE,	
Case0-3	0.031m^3s^{-1}	1 ms^{-1}	0.10	1×10^5	0.0	0°	2×10^6	107	18 cores	
Case0-4	0.031m^3s^{-1}	1 ms^{-1}	0.10	1×10^5	0.0	0°	4×10^6	223		
Case1	0.031m^3s^{-1}	1 ms^{-1}	0.10	1×10^5	0.05	3°	4×10^6	245		
Case2	0.031m^3s^{-1}	1 ms^{-1}	0.10	1×10^5	0.25	14°	4×10^6	329		
Case3	0.031m^3s^{-1}	1 ms^{-1}	0.10	1×10^5	1.00	45°	4×10^6	368		
Case4	0.031m^3s^{-1}	1 ms^{-1}	0.10	1×10^5	3.00	72°	4×10^6	421		
Case1′	0.031m^3s^{-1}	1 ms^{-1}	0.05	1×10^5	0.05	5°	4×10^6	233		
Case2′	0.031m^3s^{-1}	1 ms^{-1}	0.05	1×10^5	0.25	26°	4×10^6	351		
Case3′	0.031m^3s^{-1}	1 ms^{-1}	0.05	1×10^5	1.00	72°	4×10^6	392		
Case4′	0.031m^3s^{-1}	1 ms^{-1}	0.05	1×10^5	3.00	81°	4×10^6	467		

Table 6
Numerical schemes.

Time discretization scheme	Second-order implicit scheme	Cs number	0.1
Space discretization scheme	FVM second-order central difference scheme	SGS model	Smagorinsky-Lilly
$\Delta t W_0/D$	0.001	CFL number:	< 2
Turbulence model	Large eddy simulation	Decoupling method	SIMPLE
Time for statistics	20s	Software	Ansys Fluent 14.5

$\overline{w}_e(z)$ and $w'_e(z)$. It is clear that Case 0–3 and Case 0–4 yield very similar results for both $\overline{w}$ and w', while the difference from Case 0–1 is noticeable. Owing to the fact that the flow here is mainly laminar and the coarse grid is sufficient to capture the flow structures well, near the outlet of the chamber there appears to be negligible difference between all of the four grids, and the results are concordant with the experimental ones. Moving to the outlet of the room, the overestimation of $\overline{w}$ and w' in Case 0–1 gradually increases. On the other hand, Case 0–3 and Case 0–4 are almost identical and accurate for predicting the centerline mean and fluctuating velocities.

To clearly demonstrate the grid independence, the relative errors were analyzed as a function of the grid number. The relative errors were defined as follows. Firstly, the errors ($\varepsilon_{\overline{w}}$ for $\overline{w}$ and $\varepsilon_{w'}$ for w') were defined as the integration of the absolute difference between the simulated results and the fitted experimental curves, expressed as:

$$\varepsilon_{\overline{w}} = \int_{0.0r}^{10r} |\overline{w}_e(z) - \overline{w}(z)|dz; \quad \varepsilon_{w'} = \int_{0.0r}^{10r} |w'_e(z) - w'(z)|dz \tag{8}$$

The quantities $\varepsilon_{\overline{w}}$ and $\varepsilon_{w'}$ were then normalized by the integration of the fitted experimental curves to determine the relative errors:

$$\varepsilon_{\overline{w},r} = \frac{\varepsilon_{\overline{w}}}{\int_{0.0r}^{10r} \overline{w}_e(z)dz}; \quad \varepsilon_{w',r} = \frac{\varepsilon_{w'}}{\int_{0.0r}^{10r} w'_e(z)dz} \tag{9}$$

As shown in Fig. 4, where the relative error axis uses the logarithmic scale, the relative errors monotonically decrease with increasing the grid number and then become nearly constant (Case 3 and Case 4), 2.5%, which is sufficiently accurate for engineering applications. Therefore, we conclude that a grid with 4000,000 nodes can attain grid independence and can be considered as a suitable grid for other calculations.

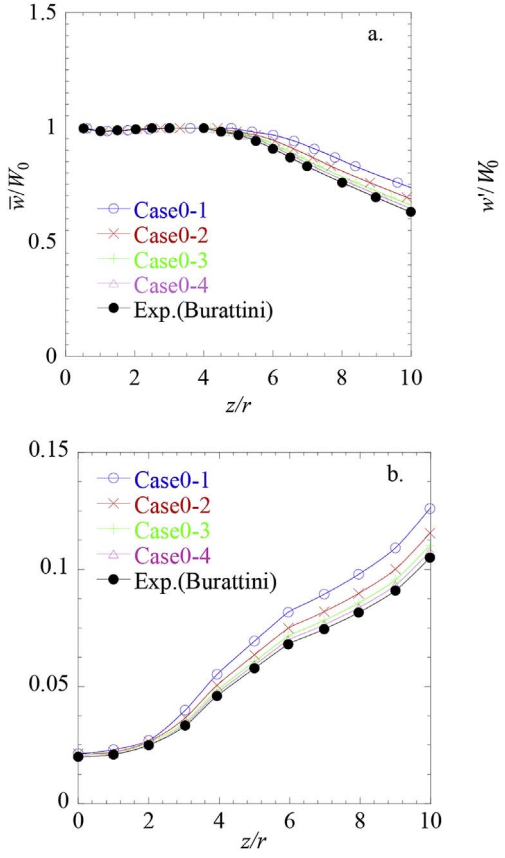

Fig. 3. Grid independency checking, (a) the mean axial velocity, $\overline{w}$, along the central line of room, and (b) rms of axial velocity, w', along the central line of room. The mean and rms of axial velocity have been normalized by W_0, and vertical location by radius of chamber outlet r. Experimental data by Burattini et al. [38] are shown with solid circles and fitted by spline curves.

3.2. Vortical structures

For the sake of specifying the main mixing characteristic in the room, a presentation of the flow vortical structures was made. Fig. 5 shows instantaneous flow structures downstream of the chamber outlet in an axonometric view. The structures are visualized by iso-surfaces of the second eigenvalue, λ_2, of a tensor M. For an incompressible flow, M is defined as:

$$M = S_{ik}S_{kj} + \Omega_{ik}\Omega_{kj} \tag{10}$$

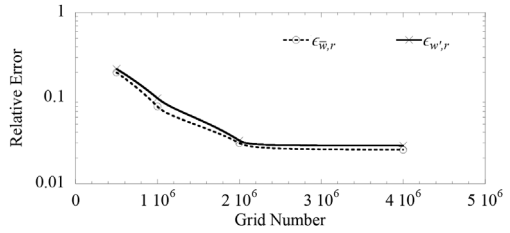

Fig. 4. Relative errors of mean axial velocity $\varepsilon_{\overline{w},r}$, and rms of axial velocity, $\varepsilon_{w',r}$, versus grid number with horizontal axis increasing linearly and vertical axis logarithmically.

where the strain-rate tensor is defined by:

$$S_{ij} = \frac{1}{2}\left(\frac{\partial u_i}{\partial x_j} + \frac{\partial u_j}{\partial x_i}\right) \tag{11}$$

and the rotation tensor is defined by:

$$\Omega_{ij} = \frac{1}{2}\left(\frac{\partial u_i}{\partial x_j} - \frac{\partial u_j}{\partial x_i}\right) \tag{12}$$

S_{ij} and Ω_{ij} represent the symmetric and antisymmetric parts of the velocity gradient tensor, respectively. Since M is real and symmetric, it

Fig. 5. Iso-surface of the second eigenvalue, $\lambda_2 = 0$, of the tensor $M = S_{ik}S_{kj} + \Omega_{ik}\Omega_{kj}$, for Case1, Case2, Case3, and Case4 at time of T1, T2, T3, and T4. Cartesian coordinates have been normalized by the radius of the chamber outlet r.

has exactly three real eigenvalues, which can be sorted according to $\lambda_1 > \lambda_2 > \lambda_3$. Vortex regions are then defined as those where $\lambda_2 < 0$, i.e., vortex boundaries are given by the iso-surfaces of λ_2 with the iso-value 0. Thus, locations in the flow where rotation dominates over strain can be revealed.

The iso-surfaces in Fig. 5 show the area of $\lambda_2 = 0$ at four consecutive time steps (T1: $t^* = 100$, T2: $t^* = 200$, T3: $t^* = 300$, T4: $t^* = 400$) of Cases 1–4. As shown Fig. 5, the evolution of the vortical structures significantly depends on the inflow angle. When the swirling strength is weak (Case 1) the vortical structure is similar to the pure straight-line jet flow. At T1, a vortex ring can be clearly identified, and the flow fields are mainly laminar. Advancing in time, the shear layer at the location about $2r$ downstream of the jet exit becomes unstable and rolls up into a series of vortex rings, and then breaks down into small vortices. Increasing the inflow angle to 14°, one can observe that the stable region of the flow becomes shorter and the turbulent zone increases. For Case 3 at T1, several secondary vortices surrounding the main vortex ring emerge and with increasing time the flow becomes unstable faster than in Case 1 and Case 2. Besides, the expansion of the turbulent region with height is noticeably larger. Further increasing φ, the throw of the diffuser seems short and the swirling flow diminishes at the middle height of the room. It can be also found that the generation of turbulence starts just at the jet exit.

Each vortical region detected by λ_2 criterion is supposed to have a rotation axis. This axis is called the vortex core line and can be defined as the connection of local pressure minima, or a connection of local λ_2 minima. The vortex core lines consist of the geometrical reduction of vortical regions to lines and provide insights about the turbulent flow structures. These lines are calculated following the method of Stegmaier et al. [39] and plotted in Fig. 6 where only the vortex core lines of the flow fields at T4 when the turbulence has developed fully are shown. The red dashed square frames, with the width of $2r$ and height of $4r$, are superimposed to indicate the region where the swirl vortex cores are obvious. For Case 1 and Case 2 it is clear that except the vortex rings there is a single vortex core in the red dashed frames. Whereas, the length of the vortex core is shortened from about $4r$ to $2r$ as the inflow angle φ increases from 3° to 14°. Interestingly, for large angle of inflow cases (Case 3 and Case 4), a two-cell vortex structure close to the jet exit appears, which shows a spiral shape. Both of the spiral shape vortex cores of Case 3 and Case 4 disappear at the vertical location around $z = 2r$. Comparing the spirals of the vortex core between Cases 3 and 4, it is found that the radius of the spiral increases with increasing the swirling strength, which indicates that the vortex core close to the jet exit is expanded. At $\varphi = 72°$, the small vortices spread almost all of the area at the outlet of the room, implying a good performance of diffusion.

3.3. Axial velocity

Firstly, the instantaneous axial velocities at T1, T2, T3, and T4 for Cases 1–4 are shown in Fig. 7, in which the horizontal and vertical axis were scaled by r and the axial velocities were normalized by the

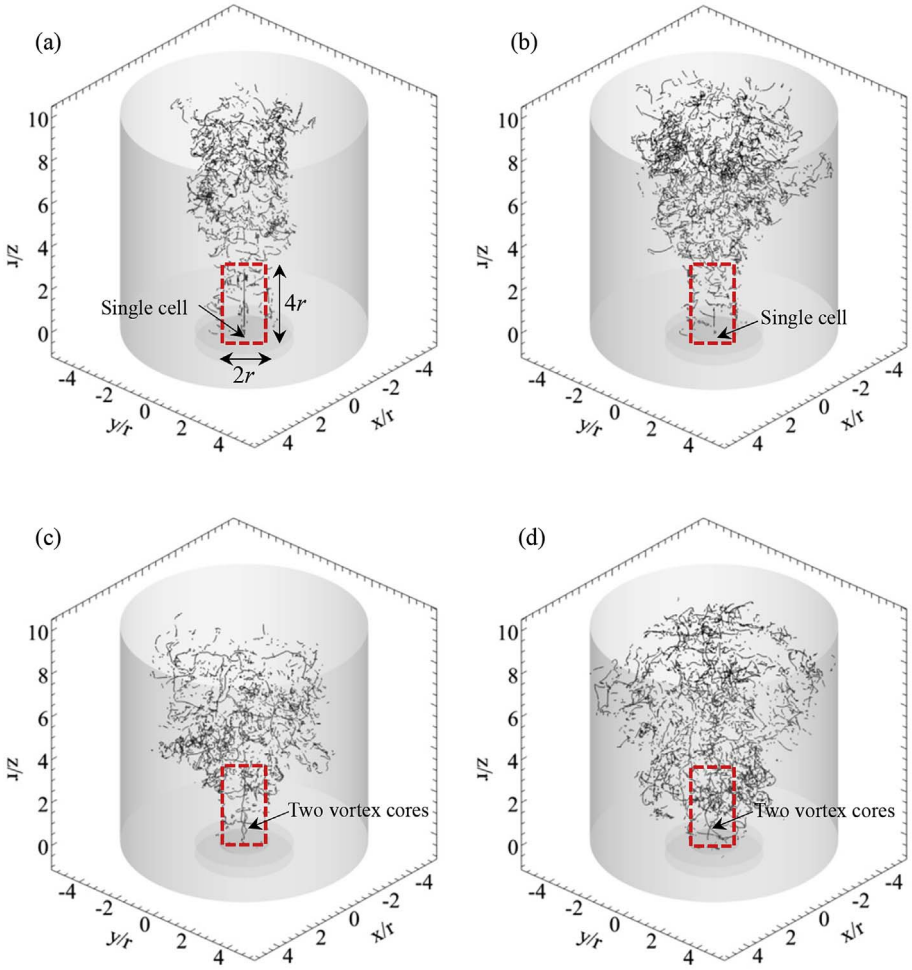

Fig. 6. Vortex core lines of (a) Case1, (b) Case2, (c) Case3 and (d) Case4 at time of T4. Red dashed square frame starts from the jet exit and ends at $z = 4r$ with a width of $2r$. Cartesian coordinates have been normalized by the radius of chamber outlet r. (For interpretation of the references to color in this figure legend, the reader is referred to the Web version of this article.)

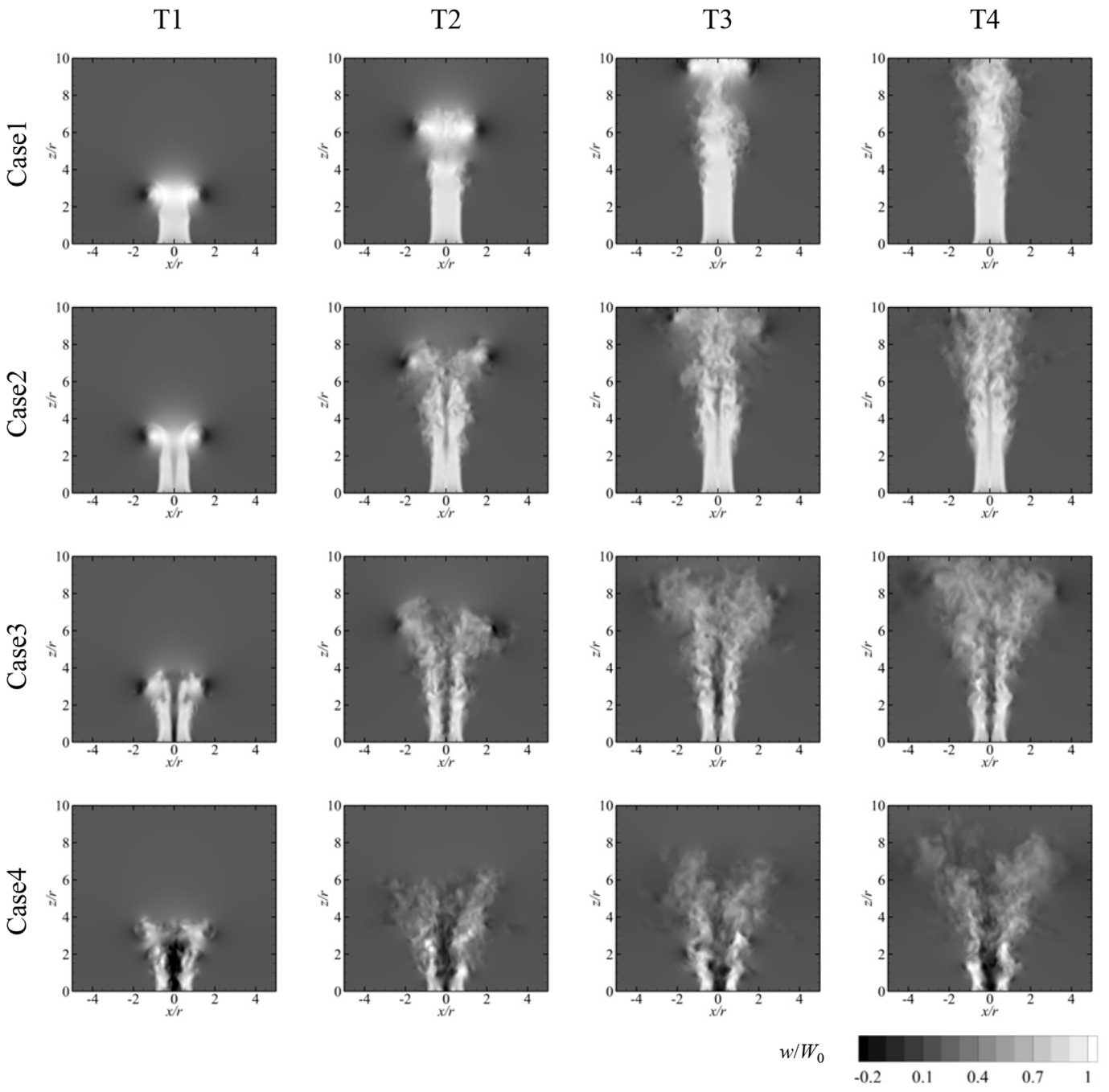

Fig. 7. Instantaneous axial velocity distribution on the central slice with horizontal and vertical axis normalized by the radius of chamber outlet r and values of the axial velocity by the averaged axial velocity at the chamber outlet W_0 at T1, T2, T3, and T4 for Case1 ~ Case4.

averaged axial velocity at the jet exit W_0. At the outlet of the room, where the pressure outlet boundary condition ($\partial p/\partial n = 0$, $\partial u_i/\partial n = 0$) was applied, the flow could move out of the computational domain freely without distinct reflections, indicating the reliability of this boundary condition. There was a remarkable difference between Case 1 and Cases 2–4. The axial velocity at the central area of the swirl jet was very small compared with the surrounding jet velocity for Cases 2–4, while the axial velocity at the center for Case 1 was always large. Furthermore, the axial velocity at the central core was in the opposite direction to the surrounding jet velocity acting as a dead flow zone. However, this zone did not appear when the angle of inflow was small, $\varphi = 3^{\circ}$. It may be owing to the fact that the swirling of the flow provided a centrifugal force $\propto V^2/R$, and in order to balance this centrifugal force a negative pressure at the central core was induced, providing a pressure gradient pointing to the center of the swirling flow. However, when the swirling strength was large, the pressure gradient could not balance the centrifugal force in the near-field region of the swirl jet flow. Consequently, the flow had to expand. It is known that tangential velocity decreases almost linearly with the expansion of flow, owing to the mass conservation. Considering the fact that the centrifugal force is proportional to V^2/R, this centrifugal force decreased with the expansion of the flow, until a new balance was reached. The detailed discussion about the momentum balance of the flow will be given in the following section. This breaking of the vortex at the center yielded the well-known vortex breakdown structure which has been observed in pipe flows [40–45] and in large-scale tornado flows in Nature [46–50]. The mixing of the flow in the far-field region strongly depended on this expansion. The contour of axial flow in center became darker as the

inflow angle φ increased, indicating that the negative axial velocity is more powerful. Owing to the expansion of the swirl flow and the resulting inner dead flow zone, it is evident that there exists another shear layer region located at the boundary of the inner dead flow zone. The additional interaction between the swirl jet flow and the inner dead flow is one of the factors contributing to the significant turbulence generated by the swirl diffuser.

The distribution of mean axial velocity, $\overline{w}$, averaged over time and Θ, is shown in Fig. 8 on the vertical slice. The yellow dashed line superimposed in Fig. 8 represents the contour lines of $\overline{w} = 0$. In this figure, the development of the break of the swirling vortex as a function of the angle of inflow is much clearer. It appears at $z = 6r$ when $\varphi = 14^{\circ}$, with the maximal width of $\sim 0.2r$. Then, the width of the vortex break increases to $\sim 0.5r$ and moves upstream of the main flow when $\varphi = 45^{\circ}$. It is interesting that in Case 4, apart from the recirculation in the near-field region of the swirl jet, another large-scale recirculation occurs in the far-field region. Looking at the outer boundary of the swirling jet flows ($\overline{w} = 0$, and $R > r$), the expansion is obvious. This expansion increases the area through which the flow passes and, considering mass conservation, the axial velocity is generally expected to decrease, which is clearly shown in Fig. 8, where the maximal axial velocity in the mainstream area at $z = 10r$ (the region enclosed by the line $\overline{w} = 0$ at $R > r$) decreases to only 80% of W_0 in Case 1 but to 10% in Case 4. In addition, the axial velocity at the room outlet shows an almost uniform distribution in Case 4, which is also important for the residents' comfort.where W_z is the axial velocity at the distance Z, and A_0 is the effective outlet area of the diffuser, $A_0 = \pi r^2$.

In addition to the discussion on the axial velocity, the jet centerline velocity decay coefficient, K, and the entrainment ratio, C_z, were further studied. The jet centerline velocity decay coefficient can be used to examine the performance of the swirl diffuser as introduced by Shakerin and Miller [51]:

$$K = \frac{W_z}{W_0}\frac{Z}{\sqrt{A_0}} \tag{13}$$

By performing linear regression, the value of K for the swirl diffuser was obtained. Note that W_z was determined by averaging the mean axial velocity over the mainstream area (the region enclosed by the line $\overline{w} = 0$ at $R > r$) considering the fact that the decay region was always referred to the fully developed flow region, the near field ($Z < 1r$) of the swirl flow was neglected. The remaining data were used to obtain K and are listed in Table 7. Table 7 shows that K is larger for larger angles of inflow. Because higher K values cause more ambient air to be mixed with the jet, we conclude that the proposed novel diffuser can create more induced air as the guide vane angle increases from 3° to 72°.

Apart from the jet decay coefficient, K, another index that characterizes the diffuser, the entrainment ratio, is also important. This index is defined as

$$\frac{Q_z}{Q_0} = C_z\frac{W_z}{W_0} \tag{14}$$

Table 7
Centerline velocity decay coefficient and mean entrainment ratio for Case0 ~ Case4.

Parameters	Case1	Case2	Case3	Case4
Centerline velocity decay coefficient (K)	0.21	0.33	0.45	0.63
Mean entrainment ratio (C_z)	1.74	1.92	2.45	4.32

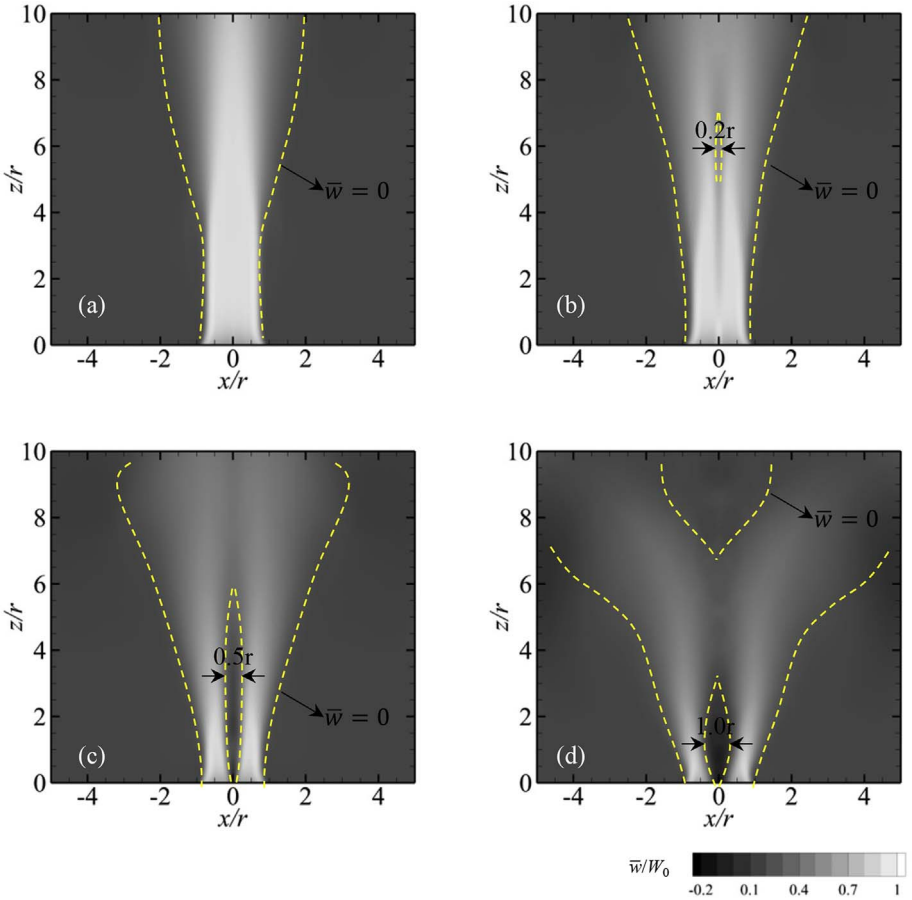

Fig. 8. Mean axial velocity (averaged in time and Θ direction) distribution on the central slice with horizontal and vertical axis normalized by the radius of chamber outlet r and values of the axial velocity by the averaged axial velocity at the chamber outlet W_0. Yellow dashed lines are the contour lines of $\overline{w} = 0$. (a) Case1, (b) Case2, (c) Case3 and (d) Case4. (For interpretation of the references to color in this figure legend, the reader is referred to the Web version of this article.)

where C_z is the entrainment ratio, Q_z and Q_0 are the airflow rate at the distance Z and the diffuser outlet, respectively. Similar to the determination of W_z at Z, Q_z is calculated by integrating W_z over the mainstream area. Therefore, C_z in the present study was actually the ratio of the mainstream area at the height of Z to that at the jet outlet, representing the extent of the swirl flow's expansion. Obviously, at almost every elevation C_z should increase with φ as can be seen from the plot of the boundary of the mainstream (yellow dashed lines in Fig. 8). And not only the value of C_z increases with φ, but also the slope of the C_z curve, indicating that the expansion of the swirl jet flow is faster for wider guide vane angles. The averaged C_z for Cases 1–4 are listed in Table 7.

3.4. Age of the air

The jet decay coefficient and the entrainment ratio as discussed in the above section in the context of the axial velocity can be used for measuring the extent to which the diffuser can deliver and circulate the air in the room, from a macro-level perspective. To obtain good insights about the quality of the ventilation process, the instantaneous age of the air should be calculated. Following the study of Tavakoli and Hosseini [24], the age of the air was determined from the following scalar transfer equation:

$$\frac{\partial \rho \tilde{s}}{\partial t} + \frac{\partial \rho \tilde{s} \tilde{u}_j}{\partial x_j} = \frac{\partial}{\partial x_j}\left(\mu \frac{\partial \tilde{s}}{\partial x_j}\right) + \frac{\partial}{\partial x_j}\left(D_t \frac{\partial \tilde{s}}{\partial x_j}\right) + S \tag{15}$$

where s is the passive scale, D_t is the turbulent molecular diffusion, and

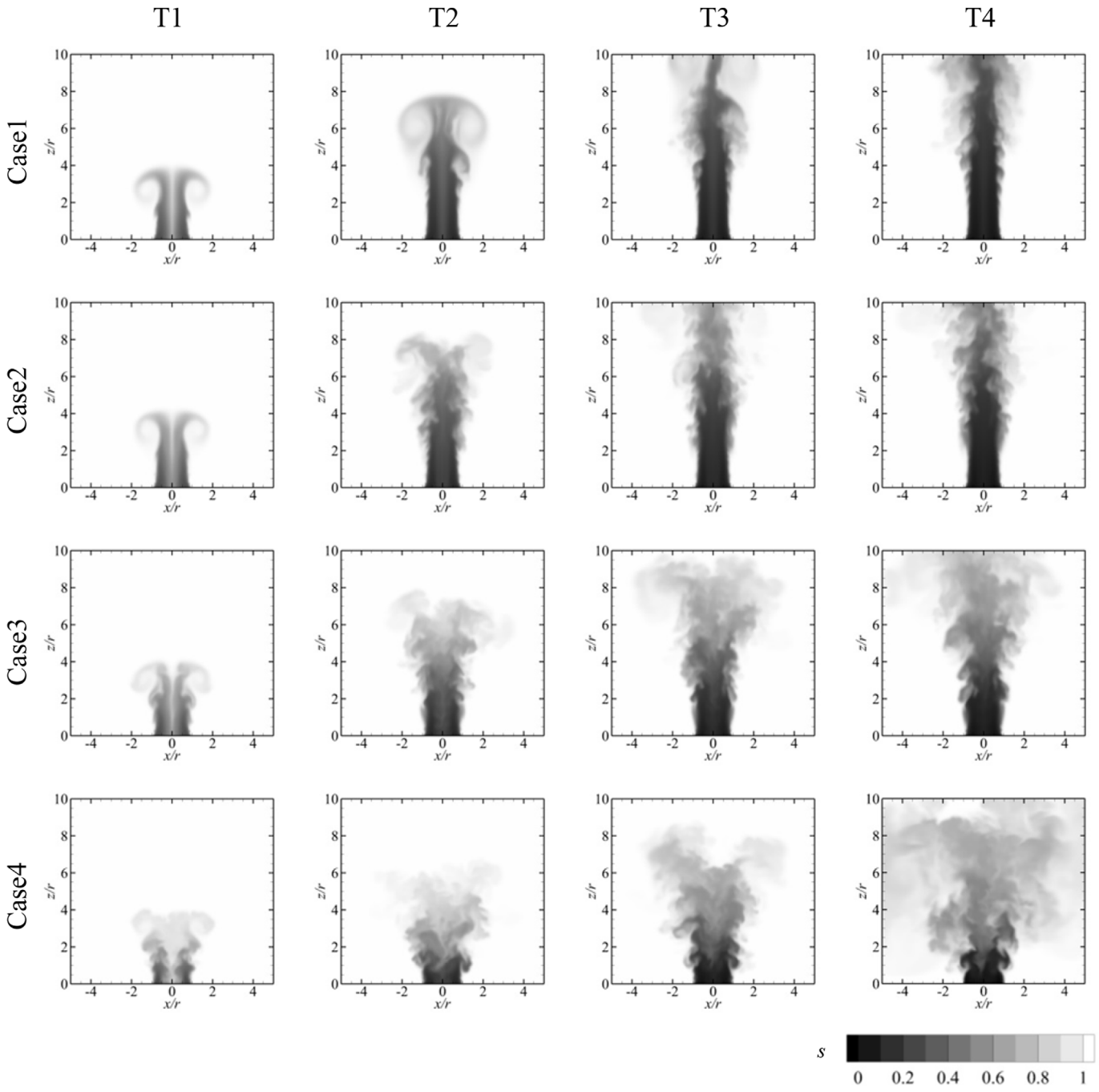

Fig. 9. Instantaneous age of air distribution on the central slice with horizontal and vertical axis normalized by the radius of chamber outlet r at T1, T2, T3, and T4 for Case1 ~ Case4.

S is the source term of the passive scale. As suggested by Tavakoli and Hosseini [24], a small source term $S = 0.002$ was used in the present study, which was sufficiently large for achieving a stationary state in a reasonable computation time and sufficiently small to allow deep penetration of fresh air. This passive scale was not directly available in Ansys Fluent 14.5; thus, it was programmed and calculated using user defined functions (UDFs) with one user defined scalar (UDS), s, determined. At the inlet of the chamber, s was set to 0, indicating fresh air, while the initial value of s in the domain was 1, indicating old air. The initial value of s and the inlet boundary condition described the situation in which a fresh air jet entered a room filled with old air. At the outlet of the room the Neumann boundary condition ($\partial s/\partial n = 0$) was applied to let the passive scalar freely move out of the computation domain.

Fig. 9 shows the transient evolution of the distribution of passive scalars during the times T1–T4 for Cases 1–4. The black color denotes fresh air, while the white color denotes old air. During T1, which marks the moment at which fresh air starts to jet from the chamber outlet, it is seen that apart from the increased turbulence in the near-field region of the swirl jet outlet with increasing φ, the distributions of s are in general similar. Different from the common straight-line jet flow, at the center of the vortex the air is old, which is probably owing to the fact that there exists a recirculation region, as shown by the above axial velocities. This recirculation region weakens the mass transfer between the inner core and the mainstream flow leaving the region with old air. With time, the differences between the cases become noticeable. It can be seen that in the stationary stage T4, the swirl jet flow with a small angle of inflow removes the fresh air out of the room without any obvious circulation or diffusion. The old air remains in the major region of the room. With increasing φ, the expansion of the vortex core enhances the circulation, and at $\varphi = 72^\circ$ the initial old air is mostly mixed with the fresh air jetting from the swirl diffuser.

Table 8
Density of the age of air in the room (S_t) and that at the outlet (S_o) for Case1 ~ Case4.

Parameters	Case1	Case2	Case3	Case4
Density of the age of air in the room (S_t)	0.97	0.85	0.76	0.63
Density of the age of air at the outlet of the room (S_o)	0.95	0.69	0.52	0.38

To examine the age of the air more quantitatively, the density of the age of the air in the room (S_t) and that at the outlet of the room (S_o) were calculated and discussed. These densities are defined as

$$S_t = \oint_{\Omega} s dv/\Omega; \quad S_o = \oint_{\Lambda} v d\Lambda/\Lambda \tag{16}$$

where Ω is the passive scalar integration volume, dv is an infinitesimal volume, Λ is the surface of the outlet over which the passive scalar integrated, and $d\Lambda$ is an infinitesimal surface. Note that in the volume integration a cylindrical zone with the radius r has been removed, and in the surface integration a circle area with the radius r has also been removed, to show the difference between the cases more clearly, as illustrated by the blue dashed lines in Fig. 10. The removal of the cylindrical zone and the circle area was motived by the consideration that the probability of having residents located just above the swirl diffuser is small, owing to its small size compared with that of the room. Fig. 10 shows the passive scale averaged over Θ in the stationary stage T4 to provide a clearer image of the distribution of the age of the air. Table 8 lists the values of S_t and S_o for different inflow angles. A significant reduction in S_t and S_o was observed, which yielded only 0.63 and 0.38, respectively, for Case 4, but 0.97 and 0.95 for Case 1, indicating the high performance of the developed swirl diffuser. In the present study, the Coanda jet flow was not observed, even for the inflow angle of 72°. Such a flow has been recognized as the optimum of a swirl jet flow

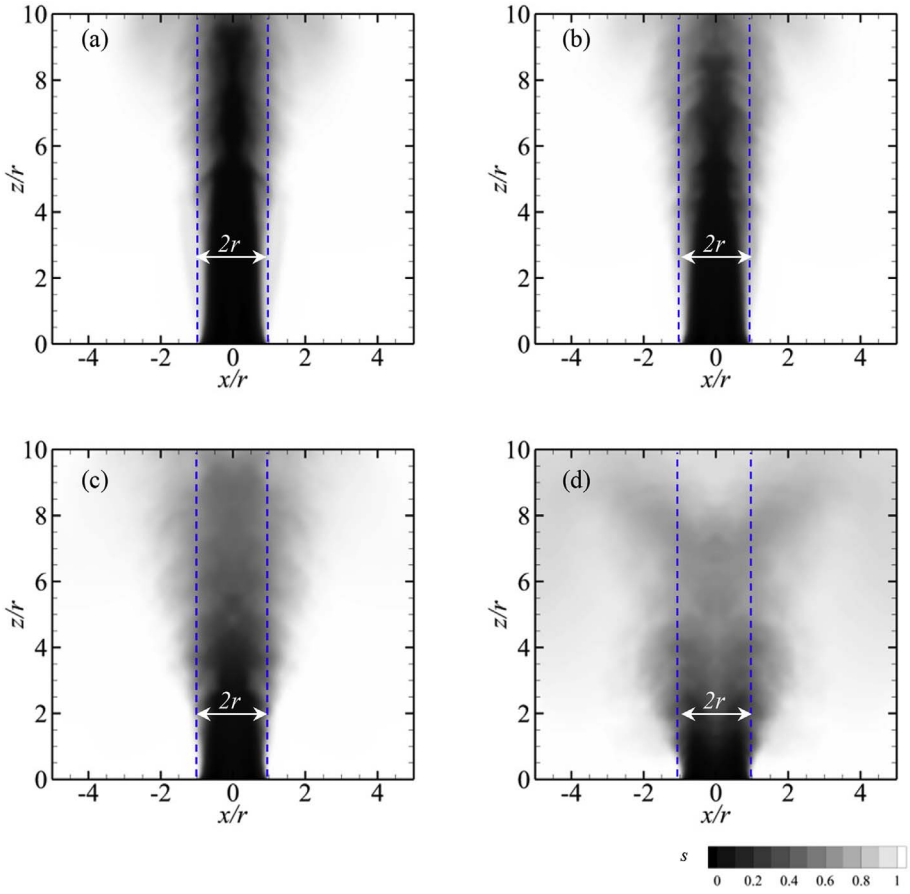

Fig. 10. Mean age of the air (averaged in Θ direction) distribution at T4 on the central slice with horizontal and vertical axis normalized by the radius of chamber outlet r. Blue dashed lines show the zone where the volume integration of the passive scalar are removed for the calculation of S_t. (a) Case1, (b) Case2, (c) Case3 and (d) Case4. (For interpretation of the references to color in this figure legend, the reader is referred to the Web version of this article.)

diffusing the air, as proposed by Sajadi et al. [12]. Therefore, the performance of the swirl diffuser in the present study could be improved by modifying some design details. Further research to address this issue will be conducted in the near future.

3.5. TKE budget

Before discussing the TKE budget, we discuss the distribution of the TKE. The TKE, $k \equiv 1/2u_i'u_i'$, is the turbulence-related component of the fluid's kinetic energy (per unit mass), $E \equiv 1/2\overline{u}_i\overline{u}_i + 1/2u_i'u_i'$, and it determines the isotropic part of the Reynolds stress tensor, characterizing the energy associated with the fluctuating velocity field. Consequently, the TKE is of considerable importance. The distribution of k, which is averaged over Θ, on the vertical slice normalized by W_0^2, is shown in Fig. 11, in which darker colors correspond to lower values and brighter ones correspond to higher values. The yellow dashed line superimposed in Fig. 11 represents the contour lines of $\overline{w} = 0$, which also indicate the shear layer locations, also shown in Fig. 8. Clearly, the TKE is concentrated in the region surrounded by the shear layers. For the low swirl strength situation (Case 1) there are two peaks located approximately at $R = 1r$, but the number of peaks increases to four when the angle of inflow increases to $\varphi = 14°$, which occurs owing to the appearance of a quiet recirculation region in the core, generating another shear layer. As can be deduced from the inner yellow dashed lines, the inner peaks of the TKE are very close to them. With the increasing swirling strength and expansion of the core size of the flow, the overall color becomes brighter, implying that the TKE increases, reaching a maximum at ~0.6 in Case 4, which occurs just above the swirl jet outlet.

The TKE budget provides information about the gain or loss of the TKE, which is formulated as:

$$\overline{u}_j\frac{\partial k}{\partial x_j} = -\frac{1}{\rho}\frac{\partial u_i'\overline{p}}{\partial x_i} - \frac{1}{2}\frac{\partial u_j'u_j'u_i'}{\partial x_i} - u_i'u_j'\frac{\partial \overline{u}_i}{\partial x_j} - \nu\frac{\partial u_i'}{\partial x_j}\frac{\partial u_i'}{\partial x_j} \quad (17)$$

where the advection term A is $-U_j\cdot\partial k/\partial x_j$, the pressure diffusion term P_r is $-1/\rho\cdot\partial u_i p/\partial x_i$, the turbulence transportation term T is $-1/2\cdot\partial u_j u_j u_i/\partial x_i$, the turbulence production term P is $-u_i u_j\cdot\partial U_i/\partial x_j$, and the dissipation term ε is $-\nu\cdot\partial u_i/\partial x_j\cdot\partial u_i/\partial x_j$. The budget is averaged over Θ, and is normalized by W_0^3/r, as shown in Fig. 12 for two elevations, $z = 2r$ and $z = 4r$.

For Case 1 at $z = 2r$ (Fig. 12(a)), throughout the swirl jet, dissipation is the dominant term, which serves as the sink of the TKE budget working against the fluctuating deviatoric stresses and transforming kinetic energy into internal energy. It is the advection that mainly balances ε. Based on the formulation of the turbulence production term, this value is mainly determined by the shear of the mean flow. In addition, the production of kinetic energy working against the Reynolds stresses removes kinetic energy from the mean flow and transfers it to the fluctuating velocity fields. As a result, the greatest production term is clearly close to the boundary of the vortex core. It peaks at $R/r = 0.7$, where the ratio P/ε is ~1/4, after which all of the budgets vanish with the radial distance. Increasing the height to $z = 4r$ (Fig. 12(b)), the balance of the turbulent kinetic energy is substantially different from that at $z = 2r$. Near the center of the flow the production term is almost zero, the same as that at the low elevation. However, the turbulent transport term emerges and balances A and ε. At $R/r = 0.7$, the production P peaks and the ratio P/ε increases to exceed 2. This TKE budget is quite similar to that of the round jet flow whose TKE budget was presented by Panchapakesan and Lumley [52], indicating weak effects from the imposed swirling of the flow. For Case 2 at $z = 2r$ (Fig. 12(c)), the budget shows almost the same balance as that for Case 1 at $z = 2r$, except the region very close to the center of the swirl jet. At

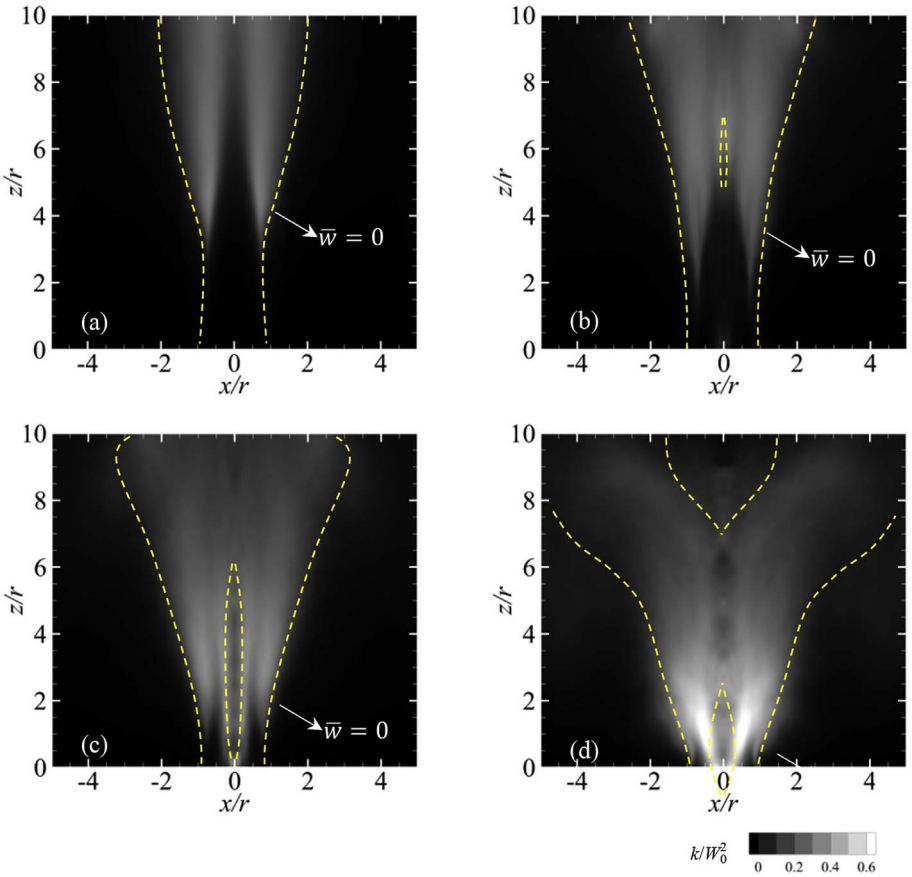

Fig. 11. TKE (averaged in Θ direction) distribution on the central slice with horizontal and vertical axis normalized by the radius of chamber outlet r. Yellow dashed lines are the contour lines of $\overline{w} = 0$. (a) Case1, (b) Case2, (c) Case3 and (d) Case4. (For interpretation of the references to color in this figure legend, the reader is referred to the Web version of this article.)

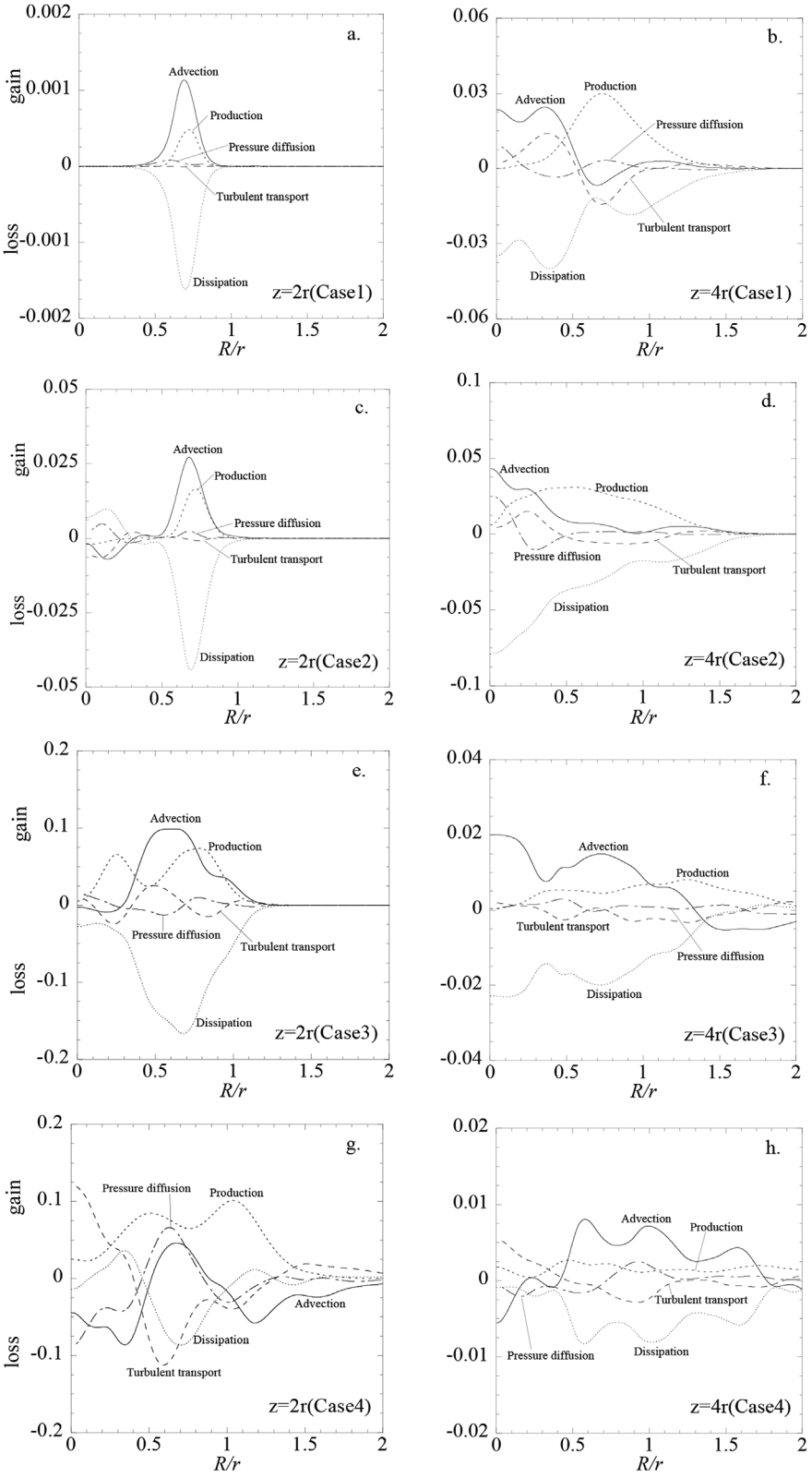

Fig. 12. Turbulent kinetic energy budget in the swirl jet averaged in Θ direction for Case1 ~ Case4 at height of $z = 2r$ and $z = 4r$. Quantities are normalized by W_0 and r.

$z = 4r$ (Fig. 12(d)), the advection as well as the dissipation decrease gradually with R and yield the main balance near the center. Halfway and further from the radius of the swirl jet outlet, the main balance is between the production and ε. Further increasing the angle of inflow to Cases 3 and 4, two obvious peaks appear in the turbulence production profile at $z = 2r$ (Fig. 12(e) and (g)), and it is noted that the peak production occurs precisely where the TKE exhibits the highest value; in other words, the region close to the boundary of the outer and inner shear layers. The dominance of advection and the relatively small amount of production, as shown in Fig. 12(f) and (h), suggest that the turbulence is strongly influenced by the conditions upstream, which means that the turbulence at $z = 4r$ is mainly owing to the convection

of the turbulence from the low elevation.

Among all of the budget terms, the production term provides the only means by which energy can be interchanged between the mean flow and fluctuations, which is the most important for the TKE budget; therefore, the distribution of P is plotted in Fig. 13, in which the scale of the contour is illustrated in the upper right corner. From the contours of P, almost the same locations between the peaks of P and that of the shear layer are clear. In addition, it is clear that the main part in the production of turbulence moves upstream with increasing the angle of inflow.

3.6. Reynolds averaged momentum balance

The force balance of the controlled volumes is useful for understanding how the pressure gradient force, the centrifugal force, the advection of momentum and the turbulent force balance each other. The balance of the Reynolds averaged Navier–Stokes equation in the radial direction in the cylindrical system of coordinates can be expressed as follows:

$$U\frac{\partial U}{\partial R} + W\frac{\partial U}{\partial Z} - \frac{V^2}{R} = -\frac{1}{\rho}\frac{\partial P}{\partial R} - \left(\frac{\partial U'^2}{\partial R} + \frac{\partial U'W'}{\partial Z} - \frac{V'^2}{R} + \frac{U'^2}{R}\right) + D_u \quad (18)$$

The left-hand side consists of the radial advection term A_{ru}, the vertical advection term A_{zu}, and the centrifugal force term C_r. The right-hand side of the equation includes the radial pressure gradient term P_r, the turbulent force term T_u, and the diffusion term D_u. The diffusion term D_u in this equation is sufficiently small to be ignored compared with the other terms. R is the radial distance away from the center ($x = 0$, $y = 0$).

The balance is shown in Fig. 14 for $z = 2r$ and $z = 4r$ for Cases 1–4 and normalized by W_0^2/r. It is clear that at the low elevation the major balance is between the centrifugal force and the pressure gradient force when the swirl strength is low, as in Case 1. This balance is broken with increasing φ as the contribution from the turbulence increases (Fig. 14(c), (e) and (f)), and the value becomes as much as 50% of the gradient force for $\varphi = 45^{\circ}$, which indicates that when the inflow angle is sufficiently large, the resulting pressure gradient force owing to the rotation of the fluid cannot balance the centrifugal force. As a result, the

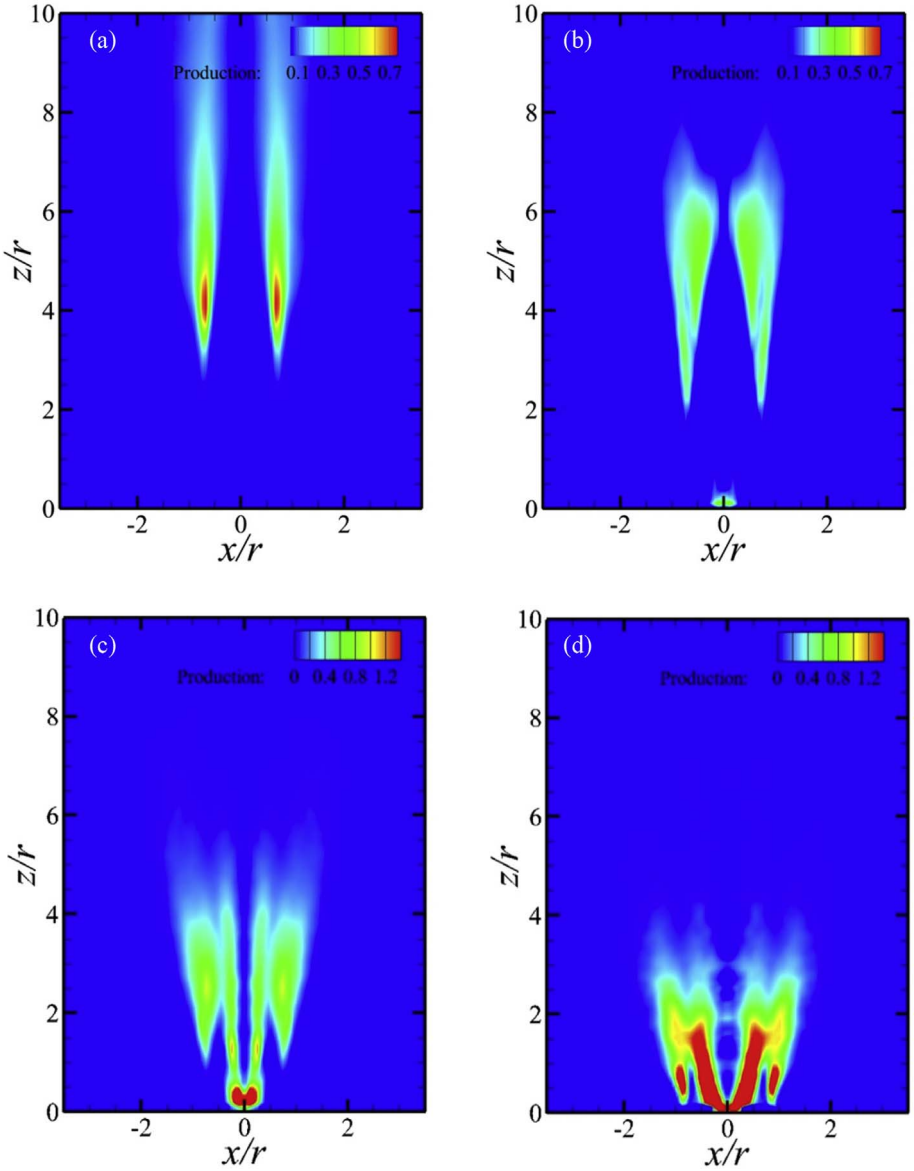

Fig. 13. Distribution of turbulence kinetic energy production averaged in Θ direction on the central slice. Quantities are normalized by W_0 and r. (a) Case1, (b) Case2, (c) Case3 and (d) Case4.

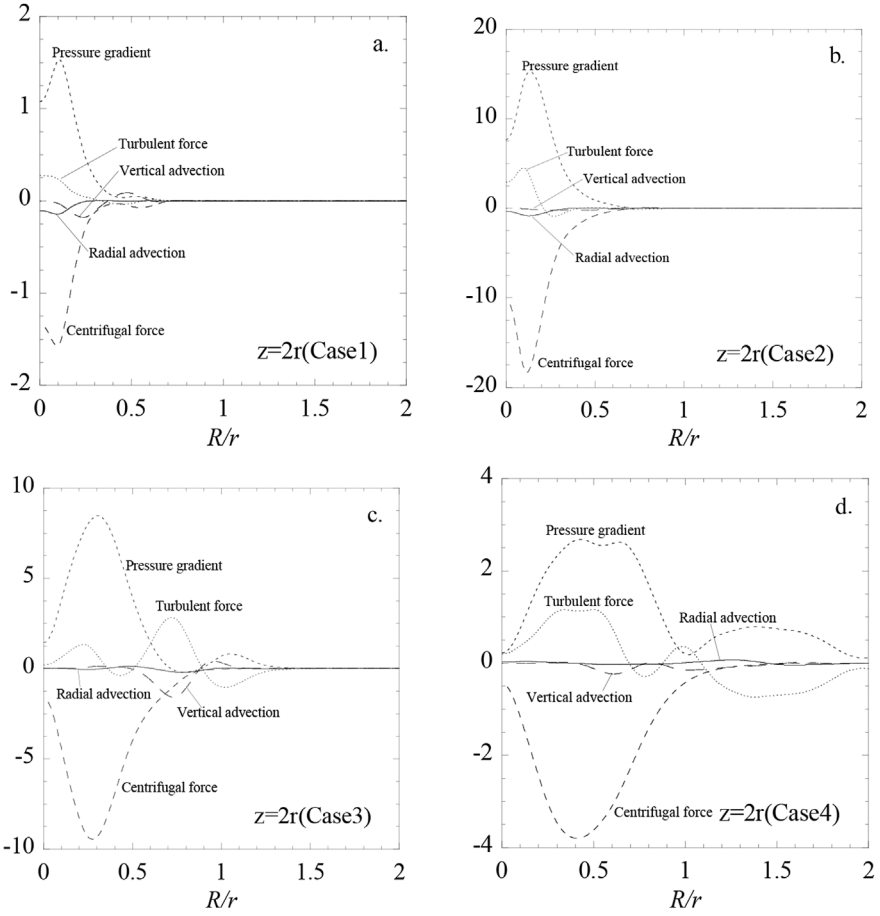

Fig. 14. The force balance in radial direction for (a) Case1, (b) Case2, (c) Case3 and (d) Case4 at height of $z = 2r$. Quantities are normalized by W_0 and r.

swirl jet breaks and forms a recirculation at the center of the jet. In addition, for Cases 3 and 4 the major balance in the outer region of the swirl jet with the low elevation is between the turbulent force and the pressure gradient force, while the contribution from the centrifugal force is almost zero.

4. Non-dimensional parameter "swirl number"

The flow structures in a swirling flow are governed by the ratio between the tangential and axial momenta at the outlet of the chamber. Several definitions have been proposed, e.g., by Grundmann et al. [53], From et al. [54], and Feyz et al. [55]. In the present study we assumed that the axial velocity at the chamber outlet is uniform and the tangential velocity, V, is proportional to r'/r. The assumption of $V \propto r'/r$ is based on checking the tangential velocity profile in the chamber. Therefore, the uniform axial velocity at the chamber outlet equals $Q/\pi r^2$, and the uniform tangential velocity at the chamber outlet equals $Q/2\pi r'h \cdot \tan\varphi \cdot r'/r$. As a result, the swirl number in the present study can be expressed as:

$$S_n = \frac{Q/2\pi r'h \cdot tan\varphi \cdot r'/r}{Q/\pi r^2} = \frac{tan\varphi}{2h/r} \tag{19}$$

The swirl number is determined by three geometrical parameters, which are the angle of inflow, φ, the height of the chamber, h, and the radius of the chamber outlet, r. In the definitions of swirl number by Grundmann et al. (2012), From et al. (2017) and Feyz et al. (2015), some of the parameters in the formulation are based on the resulted flow fields. It means that the swirl number could not be determined before the simulation or experiment. In the present formulation, all of the parameters used to determine the swirl number are the geometry parameter. It means using the formulation in the present study, the swirl number could be determined before the simulations. This is helpful for the design of the swirl diffuser. In the above discussion of Cases 1–4, only φ is modified. However, in some situations, it is much

Table 9
Representative parameters for Case1 ~ Case4 and Case1' ~ Case4'.

Parameters	Case1	Case2	Case3	Case4	Case1′	Case2′	Case3′	Case4′
Swirl number (S_n)	0.05	0.25	1.00	3.00	0.05	0.25	1.00	3.00
Centerline velocity decay coefficient (K)	0.21	0.33	0.45	0.63	0.20	0.31	0.44	0.21
Mean entrainment ratio C_z	1.74	1.92	2.45	4.32	1.71	1.89	2.39	1.75
Density of the age of air in the room (S_t)	0.97	0.85	0.76	0.63	0.98	0.87	0.65	0.61
Density of the age of air at the room outlet (S_0)	0.95	0.69	0.52	0.38	0.95	0.70	0.54	0.34

easier to change the height of the chamber, without complicating the driving devices. Thus, in this section, we ask whether or not modifying the height of the chamber could have the same effect as changing the angle of inflow. To determine whether the suggested swirl number for the proposed swirl diffuser is the key dimensionless parameter, we chose combinations of φ and h that yielded the same swirl number as the corresponding Cases 1–4. For the sake of differentiation, the cases for which the chamber height was different from that in Cases 1–4 were named Cases 1′–4′. The chamber heights in Cases 1′–4′ were set to be twice those in Cases 1–4. The parameter φ was then determined using Eq. (19) to provide the same swirl number which was much larger than those in Cases 1–4, as seen from Table 5. The decay coefficient K, the entrainment ratio C_z, the density of the age of the air in the room (S_t) and that at the outlet of the room (S_o) were calculated and compared with Cases 1–4, as shown in Table 9. Cases 1′–4′ yielded almost the same results as Cases 1–4, indicating that the swirl number is the sole dimensionless parameter determining the diffusion performance of the proposed diffuser, and changing the chamber height has the same effect as changing the angle of inflow. Changing the radius of the chamber outlet cannot be done easily owing to the many difficulties associated with the design of the driving force, limiting the scope of applications. Therefore, the effects of r were not examined in this paper.

5. Conclusions

In the present study, a swirl diffuser with a novel design was numerically studied using LES, accounting for the flow fields, the age of the air, the TKE budget, and the force balance. The following summarizes the conclusions and findings of this study:

[1] When the angle of inflow is small the vortex shows a single-cell structure. A two-cell vortex structure with a spiral shape close to the jet exit appears when the angle of inflow is large.
[2] There exists a recirculation region whose size increases with increasing the swirling strength. In this recirculation region, the air flow speed is small. Owing to this recirculation an additional shear layer appears, which is one of the main determinants of significant turbulence generated by the swirl diffuser.
[3] The centerline velocity decay coefficient, K, and the entrainment ratio, C_z, increase with increasing the swirling strength, indicating a better diffusion performance. The axial velocity at the room outlet exhibits an almost uniform distribution when the swirling strength is sufficiently large.
[4] The density of the age of air in the room and that at the outlet of the room decrease remarkably with increasing the angle of inflow, implying good mixing by the proposed swirl diffuser.
[5] The force balance analysis revealed that for sufficiently large angles of inflow the resulting pressure gradient force owing to the rotation of the fluid cannot balance the centrifugal force. As a result, the swirl jet breaks and forms a recirculation at the center of the jet.
[6] A non-dimensional parameter, the swirl number, was examined and found to be the most important parameter determining the flow structure generated by the swirling diffuser. Changing the height of the swirling diffuser chamber had the same effect as changing the angle of guide vanes.

In future studies, the proposed swirl diffuser will be further improved to reproduce the Coanda jet, which has been considered as the optimized flow structure for diffusion. The thermal effects on the air flow diffusion will be examined as well.

Acknowledgement

Supports from the National Key Research and Development Plan of China (2016YFC0800206, 2016YFE0127900), the National Natural Science Foundations of China (51608220), the Project of Innovation-driven Plan in Huazhong University of Science and Technology (2017KFYXJJ141), are gratefully acknowledged.

References

[1] F. Kuznik, G. Rusaouen, J. Brau, Experimental and numerical study of a full-scale ventilated enclosure: comparison of four two equations closure turbulence models, Build. Environ. 42 (3) (2007) 1043–1053.
[2] G. Einberg, K. Hagstrom, P. Mustakallio, H. Koskela, S. Holmberg, CFD-modelling of an industrial air diffuser-predicting velocity and temperature in the near zone, Build. Environ. 42 (3) (2005) 601–615.
[3] J.R. Fontaine, R. Rapp, H. Koskela, R. Niemela, Evaluation of air diffuser flow modelling methods experiments and computational fluid dynamics simulations, Build. Environ. 40 (3) (2005) 377–389.
[4] T. Yao, Z. Lin, An experimental and numerical study on the effect of air terminal layout on the performance of stratum ventilation, Build. Environ. 82 (9) (2014) 431–441.
[5] Y. Sun, T.F. Smith, Air flow characteristics of a room with square cone diffusers, Build. Environ. 40 (5) (2005) 589–600.
[6] H.E. Khalifa, M.I. Janos, J.F. Dannenhoffer, Experimental investigation of reduced-mixing personal ventilation jets, Build. Environ. 44 (8) (2009) 1551–1558.
[7] M.A. Aziz, I.A.M. Gad, E.S.F.A. Mohammed, R.H. Mohammed, Experimental and numerical study of influence of air ceiling diffusers on room air flow characteristics, Energy Build. 55 (2012) 738–746.
[8] P. Raftery, F. Bauman, S. Schiavon, T. Epp, Laboratory testing of a displacement ventilation diffuser for underfloor air distribution systems, Energy Build. 108 (2015) 82–91.
[9] S.C. Hu, Airflow characteristics in the outlet region of a vortex room air diffuser, Build. Environ. 38 (2003) 553–561.
[10] A. Li, C. Yang, T. Ren, X. Bao, E. Qin, R. Gao, PIV experiment and evaluation of air flow performance of swirl diffuser mounted on the floor, Energy Build. 156 (2017) 58–69.
[11] X. Wang, D.W. Pepper, Numerical simulation for under floor air distribution system with swirl diffusers, J. Heat Tran. 129 (2007) 397–403.
[12] B. Sajadi, M.H. Saidi, A. Mohebbian, Numerical investigation of the swirling air diffuser: parametric study and optimization, Energy Build. 43 (2011) 1329–1333.
[13] Y.H. Yau, K.S. Poh, A. Badarudin, A numerical airflow pattern study of a floor swirl diffuser for UFAD system, Energy Build. 158 (2018) 525–535.
[14] P.V. Nielsen, Flow in Air-conditioned Rooms, PhD thesis Technical University of Denmark, 1974.
[15] P.V. Nielsen, Fifty years of CFD for room air distribution, Build. Environ. 91 (2015) 78–90.
[16] W. Liu, J. Wen, C. Lin, J. Liu, Z. Long, Q. Chen, Evaluation of various categories of turbulence models for predicting air distribution in an airliner cabin, Build. Environ. 65 (2013) 118–131.
[17] Y. Hue, F. Haghighat, J.S. Zhang, C. Shaw, A systematic approach to describe the air terminal device in CFD simulation for room air distribution analysis, Build. Environ. 35 (2000) 563–576.
[18] E. Djunaedy, K. Cheong, Development of a simplified technique of modeling four-way ceiling air supply diffuser, Build. Environ. 37 (2002) 393–403.
[19] S. Luo, J. Heikkinen, B. Rouxa, Simulation of air flow in the IEA Annex 20 test room validation of a simplified model for the nozzle diffuser in isothermal test cases, Build. Environ. 39 (2004) 1403–1415.
[20] B. Zhao, X. Li, Q. Yan, A simplified system for indoor airflow simulation, Build. Environ. 38 (2003) 543–552.
[21] H. Awbi, Application of computational fluid dynamics in room ventilation, Build. Environ. 24 (1) (1989) 73–84.
[22] Q. Chen, Prediction of room air motion by Reynolds-stress models, Build. Environ. 31 (3) (1995) 233–244.
[23] J.M. Villafruela, F. Castro, J.F.S. José, J. Saint-Martin, Comparison of air change efficiency, contaminant removal effectiveness and infection risk as IAQ indices in isolation rooms, Energy Build. 57 (2013) 210–219.
[24] E. Tavakoli, R. Hosseini, Large eddy simulation of turbulent flow and mass transfer in far-field of swirl diffusers, Energy Build. 59 (2013) 194–202.
[25] Z. Liu, T. Ishihara, X. He, H. Niu, LES study on the turbulent flow fields over complex terrain covered by vegetation canopy, J. Wind Eng. Ind. Aerod. 155 (2016) 60–73.
[26] Z. Liu, T. Ishihara, T. Tanaka, X. He, LES study of turbulent flow fields over a smooth 3-D hill and a smooth 2-D ridge, J. Wind Eng. Ind. Aerod. 153 (2016) 1–12.
[27] J. Smagorinsky, General circulation experiments with the primitive equations, Mon. Weather Rev. 91 (1963) 99–164.
[28] D.K. Lilly, A proposed modification of the Germano subgrid-scale closure model, Phys. Fluid. 4 (4) (1992) 633–635.
[29] J. Ferziger, M. Peric, Computational Method for Fluid Dynamics, third ed., Springer, 2002.
[30] G.E. Karniadakis, S.J. Sherwin, Spectral-hp Element Methods for Computational Fluid Dynamics, Oxford University Press, 2005.
[31] P. Warzecha, A. Boguslawski, LES and RANS modeling of pulverized coal combustion in swirl burner for air and oxy-combustion technologies, Energy 66 (4) (2014) 732–743.
[32] S. Jakirlić, G. Kadavelil, M. Kornhaas, et al., Numerical and physical aspects in LES and hybrid LES/RANS of turbulent flow separation in a 3-D diffuser, Int. J. Heat Fluid Flow 31 (5) (2010) 820–832.
[33] C.S. From, E. Sauret, S.W. Armfield, S.C. Saha, Y.T. Gu, Turbulent dense gas flow

characteristics in swirling conical diffuser, Comput. Fluids 149 (2017) 100–118.
[34] A. Valera-Medina, M.O. Vigueras-Zuniga, H. Baej, et al., Outlet geometrical impacts on blowoff effects when using various syngas mixtures in swirling flows, Appl. Energy 207 (2017) 195–207.
[35] O. Bounous, Studies of the EROFTAC Conical Diffuser with OpenFOAM, Tech. Rep. Division of Fluid Dynamics Department of Applied Mechanics, Chalmers University of Technology, Göteborg, Sweden, 2008.
[36] R. Courant, K. Friedrichs, H. Lewy, Über die partiellen Differenzengleichungen der Mathematischen Physik, Math. Ann. 100 (1) (1928) 32–74 (in German).
[37] Ansys Inc, Ansys Fluent in Ansys Workbench User's Guide. U.S, (2012).
[38] P. Burattini, R.A. Antonia, S. Rajagopalan, M. Stephens, Effect of initial conditions on the near-field development of a round jet, Exp. Fluid 37 (2004) 56–64.
[39] S. Stegmaier, U. Rist, T. Ertl, Opening the Can of Worms: an Exploration Tool for Vortical Flows, Vis 05 IEEE Visualization, 2005, pp. 463–470.
[40] P. Billant, J. Chomaz, P. Huerre, Experimental study of vortex breakdown in swirling jets, J. Fluid Mech. 376 (2000) 183–219.
[41] M.R. Ruith, P. Chen, E. Meiburg, T. Maxworthy, Three-dimensional vortex breakdown in swirling jets and wakes: direct numerical simulation, J. Fluid Mech. 486 (2003) 331–378.
[42] J. Cohen, D. Mourtazin, The effect of buoyancy on vortex breakdown in a swirling jet, J. Fluid Mech. 571 (2007) 177–189.
[43] J.M. Lopez, Axisymmetric vortex breakdown Part 1. Confined swirling flow, J. Fluid Mech. 221 (1) (1990) 533–552.
[44] G.L. Brown, J.M. Lopez, Axisymmetric vortex breakdown Part 2. Physical mechanisms, J. Fluid Mech. 221 (1990) 553–576.
[45] K. Oberleithner, M. Sieber, C. N.Nayeri, et al., Three-dimensional coherent structures in a swirling jet undergoing vortex breakdown: stability analysis and empirical mode construction, J. Fluid Mech. 679 (7) (2011) 383–414.
[46] D.S. Nolan, B.F. Farrell, The structure and dynamics of tornado-like vortices, J. Atmos. Sci. 56 (1999) 2908–2936.
[47] T. Wilson, R. Rotunno, Numerical simulation of a laminar end-wall vortex and boundary layer, Phys. Fluids 29 (1986) 3993–4005.
[48] R.J. Trapp, A clarification of vortex breakdown and tornadogenesis, Mon. Weather Rev. 128 (3) (2000) 888–895.
[49] B. Fiedler, Suction vortices and spiral breakdown in numerical simulations of tornado-like vortices, Atmos. Sci. Lett. 10 (2) (2010) 109–114.
[50] D.C. Lewellen, W.S. Lewellen, Near-surface intensification of tornado vortices, J. Atmos. Sci. 64 (7) (2010) 2176–2194.
[51] S. Shakerin, P.L. Miller, Experimental Study of Vortex Diffusers, Office of Scientific & Technical Information Technical Reports (1995).
[52] N.R. Panchapakesan, J.L. Lumley, Turbulence measurements in axisymmetric jets of air and helium. part 1. air jet, J. Fluid Mech. 246 (2006) 197–223.
[53] S. Grundmann, F. Wassermann, R. Lorenz, B. Jung, C. Tropea, Experimental investigation of helical structures in swirling flows, Int. J. Heat Fluid Flow 37 (2012) 51–63.
[54] C.S. From, E. Sauret, S.W. Armfield, S.C. Saha, Y.T. Gu, Turbulent dense gas flow characteristics in swirling conical diffuser, Comput. Fluids 149 (2017) 100–118.
[55] M.E. Feyz, S.I. Pishbin, M. Ghazikhani, S.M.R.M. Razavi, Parametric assessment of a low-swirl burner using the exergy analysis, Energy 79 (2015) 117–126.